Science Bulletin 68 (2023) 1640–1650

Contents lists available at ScienceDirect

Science Bulletin

journal homepage: www.elsevier.com/locate/scib

Article

Waterwheel-inspired rotating evaporator for efficient and stable solar desalination even in saturated brine

Hanjin Jiang [a], Xinghang Liu [b], Haitao Wang [a], Dewen Wang [a], Yanan Guo [c], Dong Wang [d,*], Gang Gao [e,*], Xiaoyi Wang [f,g,*], Chaoquan Hu [a,c,f,g,*]

[a] State Key Laboratory of Superhard Materials, Key Laboratory of Automobile Materials of Ministry of Education, Jilin Provincial International Cooperation Key Laboratory of High-Efficiency Clean Energy Materials, School of Materials Science and Engineering, Jilin University, Changchun 130012, China
[b] School of Fashion and Textiles, The Hong Kong Polytechnic University, Hong Kong, China
[c] State Key Laboratory of Inorganic Synthesis and Preparative Chemistry, College of Chemistry, Jilin University, Changchun 130012, China
[d] College of Chemical Engineering, Northeast Electric Power University, Jilin 132012, China
[e] National Key Laboratory of Science and Technology on Advanced Composites in Special Environments, Harbin Institute of Technology, Harbin 150080, China
[f] Key Laboratory of Optical System Advanced Manufacturing Technology, Changchun Institute of Optics, Fine Mechanics and Physics, Chinese Academy of Sciences, Changchun 130033, China
[g] State Key Laboratory of Applied Optics, Changchun Institute of Optics, Fine Mechanics and Physics, Chinese Academy of Sciences, Changchun 130033, China

ARTICLE INFO

Article history:
Received 11 April 2023
Received in revised form 22 May 2023
Accepted 28 June 2023
Available online 10 July 2023

Keywords:
Adaptively rotating evaporator
Self-removal of salt
Waterwheel-inspired
Stable solar desalination

ABSTRACT

Solar desalination is one of the most promising technologies to address global freshwater shortages. However, traditional evaporators encounter the bottleneck of reduced evaporation rate or even failure due to salt accumulation in high-salinity water. Inspired by ancient waterwheels, we have developed an adaptively rotating evaporator that enables long-term and efficient solar desalination in brines of any concentration. The evaporator is a sulphide-loaded drum-type biochar. Our experiments and numerical simulations show that this evaporator, thanks to its low density and unique hydrophilic property, rotates periodically under the center-of-gravity shift generated by salt accumulation, achieving self-removal of salt. This allows it to maintain a high evaporation rate of 2.80 kg m^{-2} h^{-1} within 24 h even in saturated brine (26.47%), which was not achieved previously. This proof-of-concept work therefore demonstrates a concentration- and time-independent, self-rotation-induced solar evaporator.

1. Introduction

Facing severe water shortages worldwide, researchers are striving to develop sustainable desalination technology [1–3]. Interfacial solar vapor generation (ISVG) is a technology that utilizes evaporators to accelerate the vaporization of water at the interface to obtain fresh water [4–11]. Compared to traditional desalination technologies such as reverse osmosis, multi-effect evaporation and multi-stage flash evaporation, ISVG technology has the advantages of no pollution, no conventional energy consumption and high purity of fresh water obtained [12–24]. Therefore, it is considered as one of the most promising technologies to solve the shortage of fresh water. To achieve high-efficiency freshwater production, an ideal ISVG evaporator should meet the following requirements: (1) high evaporation rates over a wide salinity range (from 0% to saturated); (2) no significant decay in the evaporation rate over time; (3) low cost. However, the salt accumulation during evaporation significantly compromises the evaporation rate, making the development of high-performance evaporators extremely challenging [25–29].

Traditional evaporators are mainly static floating and combat salt accumulation through two strategies: "salt-free" and "salting-out". Employing these strategies, researchers have developed "salt-free" evaporators with Janus [30–34] and vertically aligned vessels [26,35–43] structures (Fig. 1a), and "salting-out" evaporators that remove accumulated salt by intermittent evaporation [44,45] or directional crystallization [46–51] (Fig. 1b). These evaporators have their own advantages and disadvantages. For example, "salt-free" evaporators can avoid salt precipitation, but can only operate at lower brine concentrations. The heat loss due to convection and diffusion will significantly affect the evaporation rate of the evaporators [52,53]. "Salting-out" evaporators can operate at higher brine concentrations. However, the van der Waals force between crystalline salt and the evaporator makes it difficult

* Corresponding authors.
E-mail addresses: dong.wang@neepu.edu.cn (D. Wang), gaogang930227@163.com (G. Gao), wangxiaoyi@163.com (X. Wang), cqhu@jlu.edu.cn (C. Hu).

https://doi.org/10.1016/j.scib.2023.07.011
2095-9273/

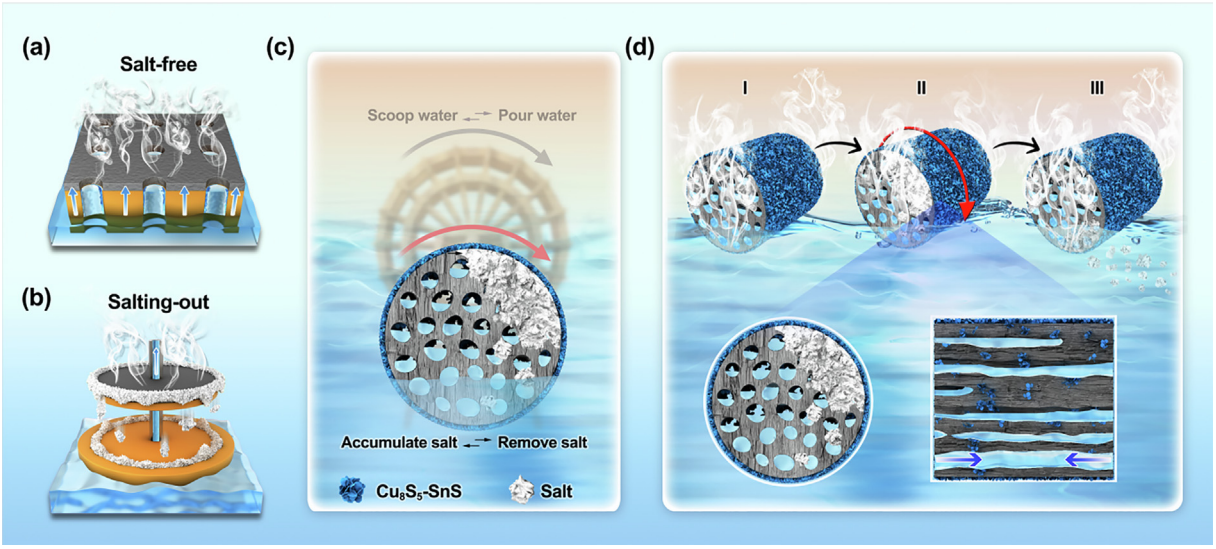

Fig. 1. (Color online) Existing salt-resistance strategies an "adaptively rotating" salt-removal strategy in this work. (a, b) Schematic diagram of the structure of a typical salt-free evaporator (a) and a typical salting-out evaporator (b). (c) Design of a rotating salt-removal evaporator inspired by waterwheels. (d) Basic working process of rotating salt-removal evaporator.

for the crystalline salt to fall off naturally and therefore timely human intervention is required, otherwise the salt encroaching on the evaporation surface will hinder evaporation [50,54]. As a result, neither the "salt-free" nor the "salting-out" evaporators can maintain efficient evaporation in high-salinity water for a long time.

To minimize the impact of salt accumulation on evaporation performance, researchers have recently developed self-rotating evaporators, which generally undergo a periodic evaporation-salt crystallization-self-refresh process. Xia et al. [55] proposed a self-rotating solar evaporator for the first time, which simultaneously achieved ultra-high salt tolerance (300 g/L) and energy efficiency (about 90%). Inspired by fish schools, Xu et al. [56] used surface tension to bring photothermal particles together and operate them simultaneously in the presence of crystallized salt. The salt production rate of the system is as high as 0.39 kg m^{-2} h^{-1}. To improve the response to accumulated salt and accelerate the evaporation surface refreshment, Wu et al. [57] developed a dual-zone photothermal evaporator that is sensitive to weight and achieved excellent salt tolerance and an evaporation rate of 2.6 kg m^{-2} h^{-1}. These studies used solar absorbers to wrap columnar or spherical heat-insulating foams to achieve continuous evaporation through two-dimensional water transmission and rotation driven by accumulated salt on the upper surface, breaking the limits of static evaporator applications.

To achieve self-rotating-cleaning, we have developed a surface hydrophobic-controllable integrated rotating evaporator through simple chemical growth. The evaporator is a Cu_8S_5-SnS loaded drum-type biochar (C/CuSnS) and its unique Janus structure and low density allow it to periodically rotate with the shift in the center of gravity to achieve automatic removal of salt. Like the "spoon water ↔ pour water" cycle of waterwheel, our evaporator rotates adaptively in the "accumulate salt ↔ remove salt" cycle, which can be used in brines of any concentration, even in saturated brine, for long-term high-efficiency solar desalination. Different from previous self-rotating evaporators, our evaporator makes use of the natural three-dimensional volume channels of wood to provide more than sufficient water for evaporation. In addition, both steam escape and salt crystallization occur on the sides of the evaporator without affecting the light absorption on the upper surface. As a result, C/CuSnS evaporator achieves a stable evaporation rate of 2.797 kg m^{-2} h^{-1} in saturated brine (26.47%). Overall, this study presents a rotating salt-removal evaporator, which blazes a new path to break through the bottleneck of salt accumulation in ISVG.

2. Materials and methods

2.1. Materials

Sodium hydroxide (NaOH), sodium sulfite (Na_2SO_3), copper acetate ($Cu(CH_3COO)_2{\cdot}H_2O$), dimethyltin dichloride (DMTC), *N*,*N*-dimethylformamide (DMF), p-phthalic acid (PTA), and sublimed sulfur were purchased from Sigma Aldrich. All raw materials were of analytical grade without any purification steps before use.

2.2. Methods

2.2.1. Pretreatment of basswood

Natural basswood with a diameter of 3 cm and a length of 4.5 cm was chosen as raw material. Firstly, the wood was rinsed with water and soaked in a solution containing 1.5 mol L^{-1} NaOH and 0.3 mol L^{-1} Na_2SO_3 at 80 °C for 5 h to remove lignin. Afterwards, the wood was repeatedly stirred and washed with deionized water until the pH reached 9. Finally, it was transferred to an oven at 60 °C for 48 h in vacuum.

2.2.2. Preparation of wood/CuSnO precursor

10 mmol $Cu(CH_3COO)_2{\cdot}H_2O$ and 10 mmol DMTC were dissolved in 100 mL of DMF solvent. The pretreated basswood was then placed in the above homogeneous solution and kept stirred for 24 h, allowing Cu^{2+} and Sn^{2+} ions to fully replace Na^+ in the wood. Next, 10 mmol of PTA and 10 mL acetic acid were added to the above wood-soaking solution. Then, the mixture was stirred thoroughly and then transferred to a 200 mL polytetrafluoroethylene-lined stainless steel reactor and kept at 120 °C for 24 h. After cooling, the blocks were rinsed three times with DMF and soaked in ethanol for 30 min to remove free materials. Finally, the wood/CuSnO precursor was obtained after 48 h drying at 100 °C.

2.2.3. Preparation of C/CuSnS desalinator

The wood/CuSnO precursor was placed downstream of the quartz tube of the tube furnace, with 0.4 g sublimed sulfur placed

upstream. Then, the furnace was heated to the specified temperature (450, 600, 750, and 900 °C) at a rate of 2 °C min^{-1} and maintained under N_2 atmosphere for 8 h to obtain C/CuSnS.

2.3. Characterizations

The morphology of carbonized wood and C/CuSnS was characterized by emission scanning electron microscopy (SEM, Hitachi SU8010). Energy dispersive X-ray spectroscopy (EDX) detected the content and distribution of elements in the material. Transmission electron microscopy (TEM) tests were carried out at 80 kV using HT7700 (Hitachi, Japan). The qualitative analysis of samples was completed by X-ray diffractometer (XRD, Bruker D8 Advance), Fourier transform infrared spectrometer (FTIR, Nexus 870), and X-ray photoelectron spectrometer (XPS, Bruker Tensor 27). The absorption spectra were detected using an ultraviolet–visible-near-infrared (UV–Vis-NIR) spectrophotometer (Shimadzu, UV-3600) with an integrating sphere. The ion concentrations in water were measured using an inductively coupled plasma optical emission spectrometer (ICP-OES, EP Optimal 8000). The hydrophilicity test of the material utilized the OCA 40 micro-volume optical contact angle measurement system. The light source of the evaporation test was the simulated natural sunlight radiated by a xenon lamp (CEL-S500/350). The intensity of the simulated solar irradiation was measured by a strong light optical power meter (CEL-NP2000-2). The real-time temperature distribution of the evaporation unit was measured by thermocouples and photographed by a FLIR E5 infrared (IR) camera.

2.4. Solar evaporation test

The solar evaporation test was performed on the self-built solar evaporation test system including simulated solar light source, electronic balance, computer, and infrared imager. The steam generation performance of the solar-driven evaporator was evaluated at an ambient temperature of ~25 °C and a humidity of ~50%.

2.5. Calculation

The evaporation rate (m, kg m^{-2} h^{-1}) is calculated according to the following formula:

$$m = \frac{\Delta m}{St}. \quad (1)$$

Here, Δm is the mass change of the liquid to be evaporated (kg), S is the projected area receiving sunlight irradiation (m^2), and t is test time (h).

3. Results and discussion

3.1. Waterwheel-inspired design of rotating evaporator

Waterwheel is a water conservancy tool in ancient China. It uses the impact of water to turn the waterwheel, which in turn drives the surrounding bamboo tubes to repeatedly scoop water to irrigate farmland. We are inspired by the "scoop water ↔ pour water" cycle of the waterwheel, and design an evaporator with an "accumulate salt ↔ remove salt" cycle. We take the gravity torque of accumulated salt as the driving force for the rotation and renewal of the evaporator, achieving the goal of the "accumulate salt ↔ remove salt" cycle (Fig. 1c). An efficient evaporator that can float and rotate at the interface needs to meet the following requirements: (1) the evaporator can transport water to the evaporation surface continuously to provide sufficient water for steam generation; (2) the evaporator should absorb as much broad-spectrum solar as possible and convert it into heat; (3) the evaporator should have a low thermal conductivity in the vertical direction to minimize heat loss to the bulk water; (4) to rotate under the gravity of accumulated salt, the evaporator should float stably at the water–air interface.

In order to meet the above requirements, we designed the following evaporator. First, we choose natural wood as the raw material, whose rich vessels and tracheids can fully pump the brine and thus fulfill the requirement (1). Then, the wood is carbonized and vulcanized to obtain a composite material of biochar and inorganic semiconductors. The composite material acts as a solar absorber with high light absorption characteristic and light-to-heat conversion capacity, which meets the requirement (2). The growth direction of the wood is parallel to the water surface when the evaporator is in operation. Natural wood exhibits a layered structure in the horizontal direction (perpendicular to the direction of growth). Abundant air pockets (tiny air gaps) are formed between the internal vessels, which can effectively reduce heat conduction loss and meet the requirement (3) [58,59]. The main material of the composite obtained during the carbonization-sulfurization process is low-density carbon, so it can float stably on the water surface, thus meeting the requirement (4). Therefore, the evaporator rotates at the interface to remove accumulated salt when the rotational torque exceeds a certain value. This ability to automatically renew the evaporation surface enables the evaporator to operate continuously and efficiently without human intervention.

The evaporator operates continuously through the cycle of salt precipitation-rotation-regeneration, which is shown in Fig. 1d. In step I, the salt solution follows a designated path into the evaporator, where the water evaporates quickly thanks to the excellent light-to-heat conversion and low heat loss of the evaporator. Meanwhile, salt starts to crystallize on the hydrophilic side of the evaporator without affecting the light absorption at the top. When the salt accumulates to a certain amount, the evaporator is triggered to rotate because of the uneven force, i.e., step II. In step III, the crystalline salt is dropped or dissolved back into the bulk water after rotation and the evaporator is regenerated.

3.2. Fabrication and characterization of C/CuSnS evaporator

Wood has natural water pumping channels and the biochar obtained by carbonizing it has low density and excellent light absorption capacity, so we choose carbonized wood as the substrate of the evaporator. However, biochar, due to its strong hydrophilicity, will quickly absorb water and submerge if placed directly on the water surface. To give the evaporator hydrophobic property and stronger light absorption capacity, we have grown semiconductor materials with micro-nano structure on the surface of biochar. First, the delignified basswood is soaked in a DMF solution containing Cu^{2+} and Sn^{2+}, and reacts at high temperature to obtain a Cu-Cu_2O-SnO_2 composite loaded wood (wood/CuSnO precursor). Then, Cu_8S_5-SnS-loaded cylindrical biochar (C/CuSnS) is further obtained in a carbonization-sulfurization reaction (see Methods for details). We perform a series of characterizations on C/CuSnS: first, the composition of the material has been analyzed and Fig. 2a and Fig. S1 (online) present the XRD patterns. The hydrothermal reaction results in a precursor comprising Cu, Cu_2O, and SnO_2, which is transformed into a Cu_8S_5-SnS composite after high-temperature vulcanization. The high-resolution TEM images (Fig. S2 online) reveal two characteristic spacings of the composite at 0.3072 and 0.3294 nm, corresponding to the (0 1 5) crystal plane of Cu_8S_5 and the (2 1 0) crystal plane of SnS, respectively. Fig. 2b is an SEM image of the outer surface of C/CuSnS, from which it can be seen that there are many nanorods with a length greater than 5 μm and coral-like nanoflowers with a diameter of about 3 μm on the outside of the carbon material. The mapping of EDX shows that the coral-like nanoflowers correspond to

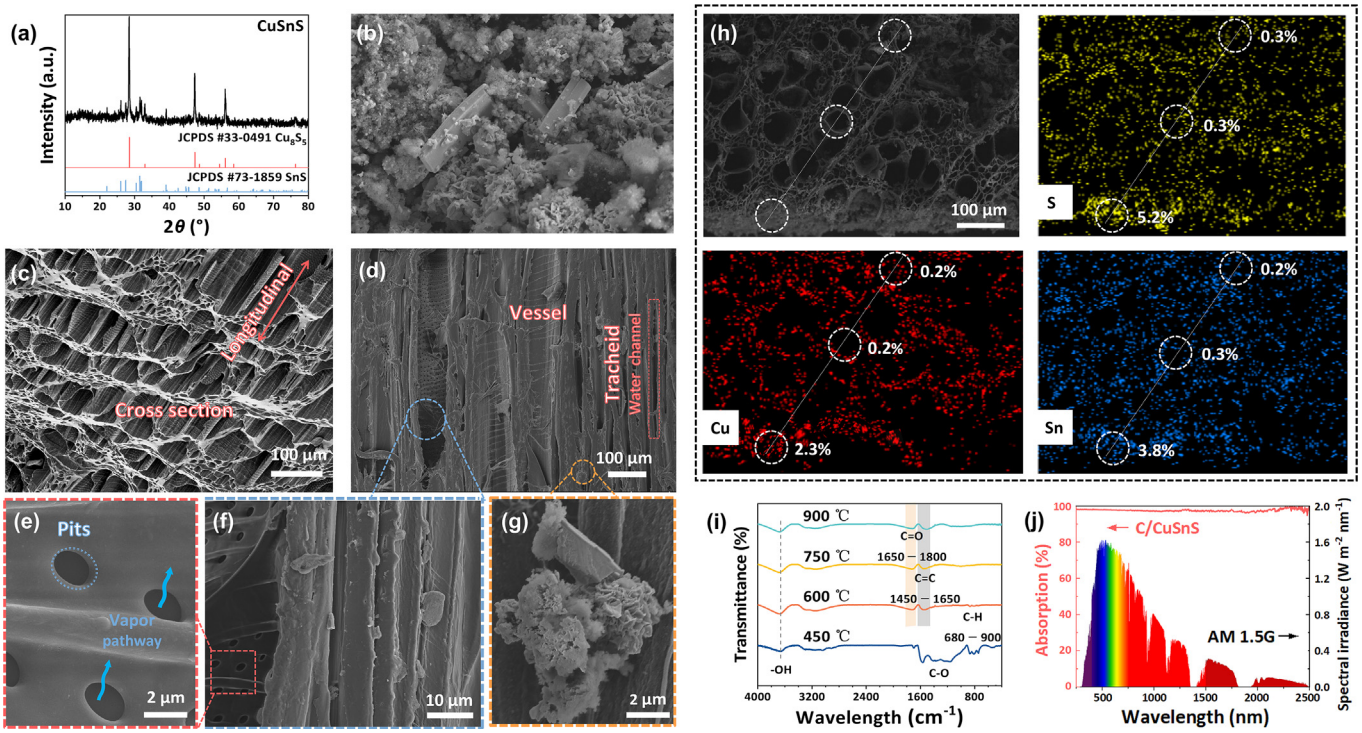

Fig. 2. (Color online) Characterization of the structure and composition of the C/CuSnS evaporator. (a) XRD patterns of semiconducting materials on biochar. (b) SEM image of semiconducting materials accumulated on the outer surface of biochar. (c–g) SEM image of C/CuSnS interior. (h) Mapping image at the edge of the C/CuSnS cross section. (i) FTIR spectra of carbonized wood at different temperatures. (j) UV–Vis-NIR absorption spectrum of C/CuSnS-600 and solar spectrum.

Cu_8S_5, while the nanorods correspond to SnS (Fig. S3 online). Then, the internal structure of C/CuSnS has been observed. As shown in Fig. 2c, carbonized wood has a unique natural hierarchical mesoporous structure with a large number of channels arranged along the growth direction inside. These channels are vessels of 50 μm in diameter and tracheids of 10 μm in diameter, which are well preserved after carbonization and can provide continuous water transport for evaporation (Fig. 2d). The junction area between channels is full of pits (about 2 μm in diameter, Fig. 2e, f). The channels and pits form a three-dimensional mass transfer network. The channels facilitate the diffusion of ions in the vertical direction (the direction of wood growth) and contribute to the equilibrium of the brine concentration; small pits on the walls of the vessel allow rapid diffusion of ions in the horizontal direction. Compared to biochar, the internal structure and channels of the vulcanized wood with Cu^{2+} and Sn^{4+} remain unchanged and a few tiny particles (Cu_8S_5-SnS) can be clearly observed attached to the channels and vessel walls (Fig. 2d, g and Fig. S4 online). At the same time, the mapping images at the edge of C/CuSnS prove that the amount of sulfide material on the outer wall is much higher than that of the inner sulfide material (Fig. 2h) as the fact that most of the inorganic raw materials accumulate on the outer wall of the wood during the cation replacement and hydrothermal reaction and only a few enter the internal pores. The outer surface of C/CuSnS exhibits hydrophobic property (the water contact angle is about 127°), while the inner part is superhydrophilic (water can be completely absorbed within 0.01 s). Therefore, we conclude that the hydrophobicity of the C/CuSnS outer wall is related to the dense Cu_8S_5-SnS composite distribution.

However, the shell of C/CuSnS is completely hydrophobic and cannot absorb water into it. To transport water into the desalinator, we rubbed off 2 mm of the flat surfaces at both ends of the C/CuSnS with sandpaper to expose the hydrophilic part (Fig. S5 online). In this way, the C/CuSnS desalinator can absorb water efficiently. When the evaporator is placed on the water surface, the part below the gas–liquid interface absorbs water and then gradually transports it above the interface for evaporation, allowing the water content of the evaporator to reach a dynamic balance (Fig. S6 online). Therefore, during evaporation, the evaporator has a wetting gradient in the direction perpendicular to the water surface. This not only ensures the water supply for evaporation, but also ensures that the evaporator floats stably on the water surface. Unsurprisingly, biochar, C/CuSnS, and polished C/CuSnS cylinders exhibit significant differences in water evaporation rates under the same test conditions (Fig. S7 online). Among them, the evaporation rate of the polished C/CuSnS desalinator is three times higher than that of the other two.

The above results demonstrate that we have synthesized C/Cu_8S_5-SnS composite material. Cu_8S_5-SnS micro-nano materials diffuse from outside to inside on the biochar, forming a special distribution gradient with more outside and less inside. Biochar, as the substrate of the evaporator, not only transports water for evaporation but also features excellent light absorption capacity [60–64]. Copper sulfide is a common light-to-heat conversion material [65]. The Cu_8S_5 nanoflowers here are agglomerated by many sheets, which can reflect the incident light multiple times and improve the utilization rate of solar energy [66,67]. SnS, as a common hydrophobic nanomaterial, can achieve the controllable adjustment of the hydrophobicity of the material [68,69].

To achieve the ultimate goal of efficient evaporation, we adjusted different carbonization temperatures and discussed the effect of carbonization temperature on the composition of carbon materials. Fig. 2i is the FTIR spectra of carbonized wood at different temperatures. After carbonization at 450 °C for 8 h, the absorption peaks between 1100 and 1300 cm^{-1} prove the existence of various C-O bonds and multiple aromatic inter-disubstituted C-H out-of-plane vibration absorption peak are evident at 874, 809, and 744 cm^{-1}. When the carbonization temperature is increased to

600 °C, the characteristic absorption peaks of C-O and C-H disappear and the peak of unsaturated C=C bond appears around 1450–1650 cm^{-1}. Due to the weak electron bonding strength of the π bond in the double bond, only a small amount of energy is needed to excite electrons from the π orbital to the π* orbital. The presence of π bonds in the material enables electrons to be excited by nearly every wavelength of the solar spectrum, resulting in light absorption. However, for single bonds such as C-C, C-O, C-H, etc., there is a large energy gap between σ and σ* orbitals, corresponding to light wavelengths below 350 nm, so σ-σ* transitions cannot be achieved in sunlight. Therefore, the presence of C=C bond contributes to the light absorption of the material [61,70–72]. To verify this issue, we have tested the UV–Vis-NIR absorption spectra of materials obtained at different carbonization temperatures. The absorption spectra indicate that the carbonized wood has a high light absorption capacity (96.93%) in the broad solar spectrum. The CuSnS nanoparticles growing on the surface of biochar improve the utilization of solar radiation, especially the absorbance in the high intensity ultraviolet–visible band of the standard spectrum (AM 1.5G) on the Earth's surface. Among them, C/CuSnS-600 exhibits the highest solar spectrum absorption efficiency (98.03%), which is consistent with the FTIR results (Fig. S8 online and Fig. 2j). This strong light absorption can be attributed to two aspects. Both C and Cu_8S_5 components in the composite have excellent photon harvesting capability [72–74]. The well-retained layered porous structure of wood after carbonization will produce multi-level reflection of incident light and improve light utilization efficiency (Fig. 2c). However, when the carbonization temperature is increased above 750 °C, the internal structural damage caused by high temperature will disrupt the internal structural regularity of biochar, thus weakening the multi-level reflection of light inside (Fig. S9 online). The light absorption performance of C/CuSnS-600 is superior to that of most reported composite evaporators based on wood or other biomass, which provides a sufficient prerequisite for ISVG (Fig. S10 online).

3.3. Efficient evaporation for a wide salinity range

3.3.1. Vapor and fresh water generation performance

We systematically investigated the steam generation performance of a C/CuSnS floating rotating evaporator (FR-evaporator) obtained by vulcanization reaction at different temperatures in deionized water, with pure water and carbonized wood as control groups. Fig. 3a demonstrates that without any evaporator assistance, the cumulative mass change of pure water under one sun irradiation for 1 h is only 0.38 kg m^{-2}. The water evaporation rate driven by floating biochar is 1.51 kg m^{-2} h^{-1}, which can be attributed to the excellent water transport and light absorption capacity of carbonized wood. However, the 1 h cumulative water mass loss of the C/CuSnS FR-evaporator can reach 2.12–2.76 kg m^{-2}, with C/CuSnS-600 exhibiting the highest water evaporation rate (7.26 times that of pure water). Therefore, we adopt C/CuSnS-600 as the material of the evaporator in the following experiments. In addition, we place the evaporator vertically with the water surface in the traditional evaporation manner to form a static vertical evaporator (SV-evaporator). Because of the better vertical water supply channel and direct evaporation from the irradiated surface, the SV-evaporator can achieve an evaporation rate of 3.28 kg m^{-2}-h^{-1} (Fig. S11 online). The main reasons for such a high rate of ISVG achieved by the C/CuSnS evaporator include: first, C/CuSnS has extremely high solar absorption, giving the evaporation system sufficient initial energy input. Second, the natural vessels and tracheids of the wood are well preserved inside the evaporator, which allows for a rapid water supply. Third, the temperature of the side evaporation plane is always lower than the ambient temperature (Fig. 3b), and additional energy can be obtained from the environment through thermal radiation and convection. The analysis of the energy flow of the evaporator during operation is shown in Fig. S12 (online). The energy harvested by the SV-evaporator from the environment is calculated to be about 11.15 mW (Table S1 online).

To match the results of desalination in reality, we have tested FR-evaporator's ability to treat brine under the same conditions. With 15 wt% brine for example, C/CuSnS-600 still exhibits the best water evaporation performance (2.36 kg m^{-2} h^{-1}, Fig. 3c), which is lower compared to that of deionized water because of the higher saturation vapor pressure of the brine. Next, we have condensed and collected the vapor generated by the evaporation of 15 wt% brine, and measured the Na^+ concentration in the condensed water. The results show that the salt concentration has dropped from 150 g/L before evaporation to about 0.83 g L^{-1}, meeting the drinking water quality standards of the World Health Organization (WHO) and the Environmental Protection Agency (EPA) (Fig. 3d), which confirms the effectiveness of the C/CuSnS FR-evaporator for desalination. In Fig. 3e, we compare the 24 h average evaporation rate of the C/CuSnS FR-evaporator with that of the reported solar desalinators [36–39,46,52,75–84]. The traditional desalinators have high evaporation rates, and are more suitable for "the applications with low salt concentration where fresh water is required in a short time". However, our research is not restricted by concentration and time and is therefore more suitable for "applications with high salt concentration where continuous operation is required over a long period of time". In addition to desalination, C/CuSnS evaporator can also be used to obtain fresh water from industrial and agricultural wastewater. To explore the potential of FR-evaporator in wastewater treatment, we have investigated its water evaporation performance under extreme conditions (strong acidity and strong alkalinity). Fig. S13 (online) illustrates that C/CuSnS can remain intact and float stably in acidic and alkaline solutions. Under one sun irradiation, its evaporation capacity for 1 mol L^{-1} HCl and NaOH solutions is barely reduced compared to that for deionized water (Fig. 3f). Since the rich copper ions and tin ions on the surface of the evaporator can coordinate with the chloride ions in the hydrochloric acid solution, the number of solute particles in the solution is reduced. Depending on the colligative property of dilute solutions, the vapor pressure of HCl solution decreases, so the evaporation rate is slightly higher than that of NaOH solution [85–88]. The stable evaporation in brine, HCl solution, and NaOH solution can be attributed to the mechanical and chemical stability of the C/CuSnS composite. The above results prove that the excellent freshwater acquisition ability of C/CuSnS FR-evaporator makes it highly promising for applications in desalination and sewage treatment.

3.3.2. "Adaptively rotating"—for efficient and stable desalination

Rapid steam generation is often accompanied by significant salt accumulation during solar desalination. And the higher the salinity of the water to be treated, the faster the salt accumulation. The salt accumulation on the evaporation surface and in internal channels seriously hinders solar energy harvesting, water transport, and steam escape, thus significantly reducing the evaporation efficiency and operating time of the evaporator. The C/CuSnS SV-evaporator, for example, the evaporator is placed in 15 wt% brine and irradiated by simulated sunlight of 1 kW m^{-2}. After 2 h evaporation, salt crystals appear on the upper surface of the SV-evaporator. The crystalline salt increases rapidly with time until the evaporation surface is completely covered (Fig. S14 online). Therefore, the SV-evaporator could not maintain long-term evaporation in brine, although it exhibits a high rate of evaporation at the start. In this study, different concentrations of brine (5 wt%, 10 wt%, 15 wt%, 20 wt%, and saturated NaCl solutions) have been used to demonstrate the salt tolerance of the C/CuSnS

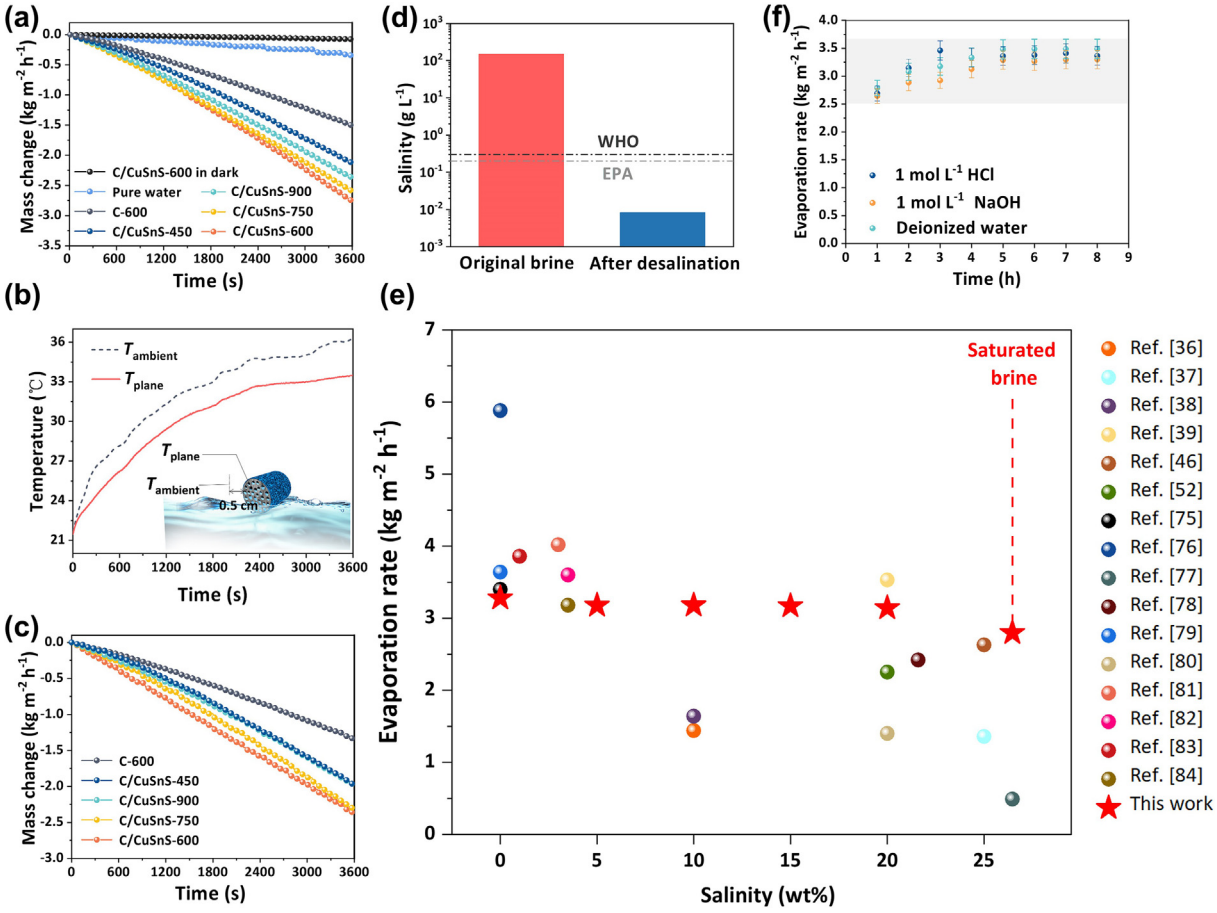

Fig. 3. (Color online) Water evaporation and freshwater generation performance of C/CuSnS FR-evaporator. (a) Mass changes of deionized water over time, including pure water (with no evaporator), C-600, C/CuSnS-450, C/CuSnS-600, C/CuSnS-750, and C/CuSnS-900, under one sun irradiation and dark conditions. (b) The curves of the changing evaporation surface temperature and the ambient temperature during the operation of the FR-evaporator. (c) Mass changes of 15 wt% brine under one sun condition within 1 h, with C-600, C/CuSnS-450, C/CuSnS-600, C/CuSnS-750, and C/CuSnS-900 as evaporators. (d) Difference in salinity of initial water and condensate from solar desalination. (e) Comparison of salinity of treated water and evaporation rate under one sun irradiation between the C/CuSnS FR-evaporator and the reported system. (f) Changes in the evaporation rate of the FR-evaporator for evaporation of acidic and alkaline solutions for 8 h.

FR-evaporator in ISVG. Since the sun that rises in the east and sets in the west is in constant motion (the azimuth of the sun varies between 0°–90°), here we irradiate the simulated sunlight on the evaporator at an angle of 45° to the water surface. Under 1 kW m^{-2} sunlight, the FR-evaporator is floated on the surface of solutions with different salinities to drive evaporation for 24 h. It can be seen from Fig. 4a that the evaporation rate of the FR-evaporator fluctuates within 24 h. Salt crystals appear on the hydrophilic surfaces at both ends of the FR-evaporator, and accumulate continuously as evaporation progress. During this process, the evaporation rate of the FR-evaporator drops slightly. However, as the mass of accumulated salt increases, the rotational inertia of the FR-evaporator increases until it breaks the balance between gravity and buoyancy and the FR-evaporator rotates. The gravity of the accumulated salt serves as the kinetic energy to drive the evaporator to rotate. The rotation of evaporator enables the crystallized salts to be sent back to the bulk water or redissolved (Video S1 online). The evaporator is then regenerated and its evaporation rate returns to the initial level (Fig. 4b). The fluctuations in evaporation rate are induced by the FR-evaporator's salt precipitation-rotation-regeneration cycle. However, the evaporator still maintains excellent performance despite these fluctuations. The 24 h average evaporation rates of FR-evaporator for 5 wt%, 10 wt%, 15 wt%, 20 wt%, and saturated brine are 3.178, 3.180, 3.170, 3.142 and 2.797 kg m^{-2} h^{-1}, respectively (Fig. S15 online). Each background color replacement in Fig. 4a represents a rotation-update of the FR-evaporator. It is noteworthy that the higher the salt concentration, the shorter the time required for a salt precipitation-rotation-regeneration cycle of the FR-evaporator, and the stronger the desalination effect. Therefore, the FR-evaporator can rotate adaptively in water with different salinities, and maintain a high water evaporation rate without human intervention. In order to better visualize the rotation of the FR-evaporator driven by salt accumulation, we have taken photos of the evaporator during the 24 h process of treating saturated brine (Fig. 4c). It can be noted that the salt precipitated on the hydrophilic surface of the FR-evaporator is always uneven because of the non-vertical irradiation of simulated sunlight. The FR-evaporator rotates every 180–210 min in saturated brine. At a salt concentration of 15 wt%, both the salt deposition rate and the evaporator rotation frequency decrease (Fig. S16 online), but the evaporator still maintains efficient and stable evaporation. The above results prove that the FR-evaporator is capable of adaptive desalination, and can maintain efficient evaporation through rotation-regeneration in water with a wide range (from 0% to saturated) of salt concentrations.

Fig. 4d shows the hourly curves of the changing average evaporation rate of FR-evaporator and SV-evaporator during 24 h evaporation of saturated brine under one sun. The evaporation rate of the SV-evaporator decreases sharply from the third hour because of salt accumulation, while the FR-evaporator features better

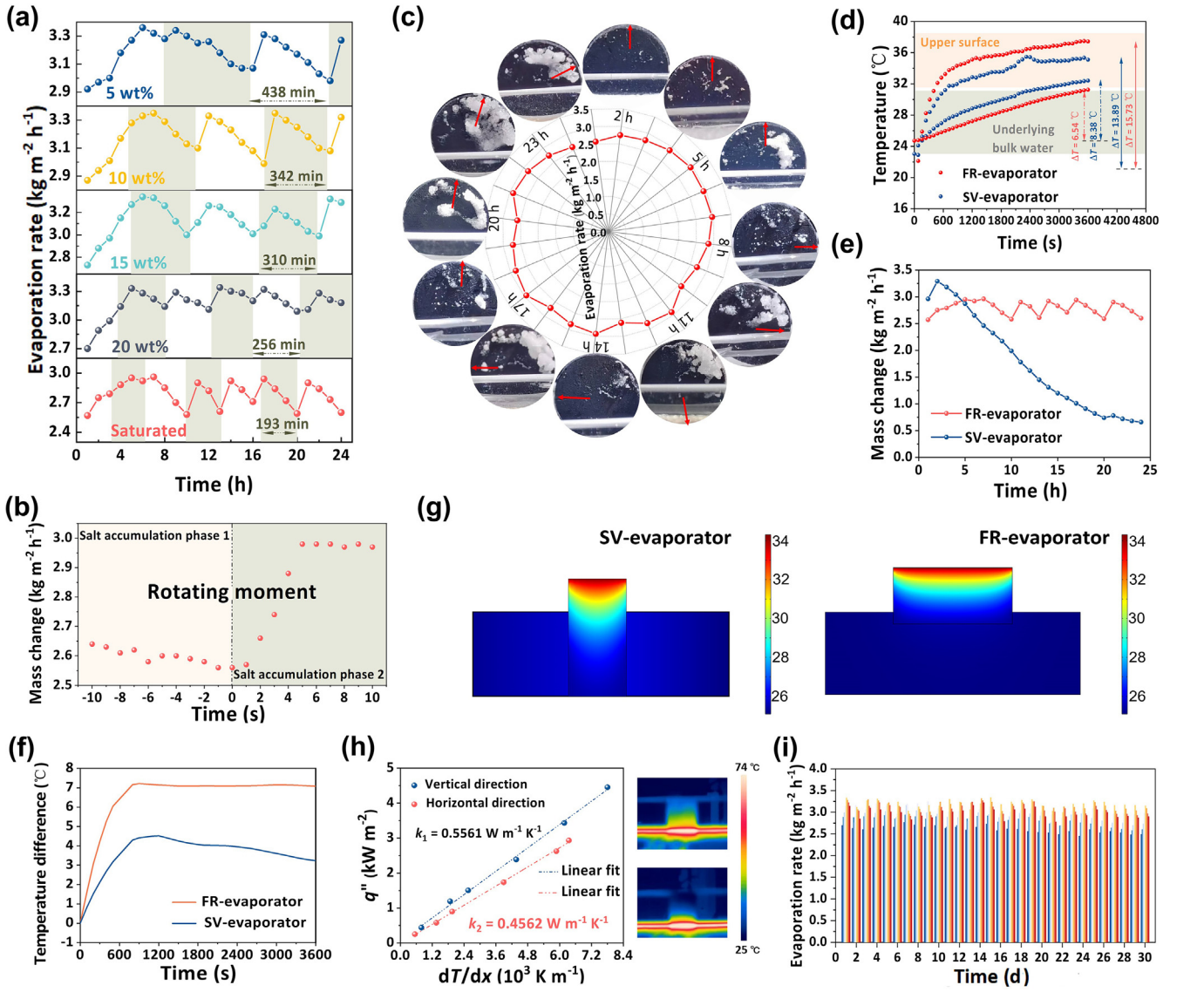

Fig. 4. (Color online) Efficient and stable evaporation driven by "adaptively rotating" of C/CuSnS FR-evaporator. (a) Evaporation rate curves of the C/CuSnS FR-evaporator in 5 wt%, 10 wt%, 15 wt%, 20 wt%, and saturated brine for 24 h. (b) Instantaneous evaporation rate curves of 10 s before and 10 s after FR-evaporator rotation. (c) Salt accumulation photos of an evaporation surface of FR-evaporator during 24 h evaporation in saturated brine. (d) Comparison of evaporation rates of FR-evaporator and SV-evaporator in saturated brine within 24 h. (e) Temperature changes of the light absorbing layer and underlying bulk water of FR-evaporator and SV-evaporator under one sun illumination within 60 min. (f) The temperature difference between the evaporation surface and bulk water of the FR-evaporator and SV-evaporator simulated by COMSOL Multiphysics respectively. (g) 3D steady-state simulation of the temperature distributions of FR-evaporator and SV-evaporator. (h) Thermal conductivities and infrared images of FR-evaporator and SV-evaporator. (i) Long-term evaporation rates (30 days, 8 h per day) of FR-evaporator in 20 wt% brine under one sun.

long-term stability in saturated brine due to its rotation-regeneration capacity. After 24 h, the cumulative evaporation of FR-evaporator in saturated brine is 66.90 kg m^{-2}, while that of SV-evaporator is only 41.72 kg m^{-2} (Fig. S17 online). With longer working time, the comparative advantage of FR-evaporator will be more obvious. In addition to the rotation-regeneration capacity, the FR-evaporator also has advantages in thermal localization, which is also crucial to efficient evaporation. Under one sun irradiation, the upper surface temperature of the FR-evaporator rapidly increases to 30 °C in approximately 6 min, and finally reaches a steady-state temperature of more than 37 °C. In contrast, the final evaporation temperature of the SV-evaporator is 35 °C (Fig. 4e). Moreover, the underlying bulk water temperature of FR-evaporator and SV-evaporator increases by 6.54 and 8.38 °C, respectively, for the same bulk water volume. The corresponding heat conduction losses are 43.51 and 66.19 mW, respectively (Table S1 online). We simulated the temperature distribution of the FR-evaporator and SV-evaporator evaporation systems using COMSOL (Fig. 4f, g). As shown, the simulation results are in good agreement with the experimental results in Fig. 4e, demonstrating the better thermal localization capability of the FR-evaporator. The difference in thermal localization is attributable to the structural anisotropy of wood, i.e., the difference in thermal conductivity in different directions. Fig. 4h shows the results of the thermal conductivity test for C/CuSnS. In the vertical direction, the evaporator has a thermal conductivity (wet state) of 0.5561 W m^{-1} K^{-1} and thus transfers more heat to the underlying water. In the horizontal direction, C/CuSnS has a lower thermal conductivity in the wet state (0.4562 W m^{-1} K^{-1}) because of the layered structure formed by abundant channels. Therefore, the FR-evaporator performs better in heat localization and the heat generated by light-to-thermal conversion can be more effectively used for the vaporization of

water. This is also evidenced by infrared photos taken during evaporation, as presented in Fig. S18 (online). The cycle stability of the FR-evaporator is also explored. It is exposed to one sun for 8 h per day in 20 wt% brine. After 30 days, the 8 h average evaporation rate of the FR-evaporator is 2.86 kg m^{-2} h^{-1}, which decreased by only about 8% (Fig. 4i).

3.3.3. Outdoor fresh water collection

After the successful indoor experimental demonstration, we further conducted a real solar-driven evaporation test to evaluate the water harvesting capability of the FR-evaporator in natural environments. An outdoor evaporation device is constructed that allows simultaneous evaporation–condensation-fresh water collection. The water inside the evaporation device can be replenished in real time without disassembly. The device works continuously for 9 h (8:00–17:00) under outdoor sunlight, as shown in Fig. 5a–c. During this period, solar irradiation is carefully tracked hourly using a portable pyranometer, and real-time ambient temperature and freshwater collection production are also recorded. Fig. 5d shows freshwater production as a function of ambient temperature and solar intensity. At an average ambient temperature of 23.3 °C and an average solar intensity of 538.4 W m^{-2}, the cumulative freshwater production of the FR-evaporator is 4.11 kg m^{-2}, with an average yield of 1.22 kg m^{-2} h^{-1}. The maximum freshwater collection rate is 1.83 kg m^{-2} h^{-1} (12:00–13:00), confirming the reliability of the FR-evaporator for desalination in practical conditions.

4. Conclusion

Inspired by the "scoop water ↔ pour water" cycle of waterwheel, we have prepared an adaptive C/CuSnS FR-evaporator capable of continuous operation of "accumulate salt ↔ remove salt", which can achieve efficient and stable solar desalination in a wide range of salt concentrations (from 0% to saturated). The FR-evaporator is synthesized by simultaneous carbonization-vulcanization method and simple mechanical grinding. Taking advantage of wood's natural water transmission channels and layered structure, it has outstanding water supply and heat localization capabilities. The FR-evaporator removes salt using the gravity of accumulated salt as the driving force for rotation and its rotation-regeneration period decreases as the salt concentration increases. Therefore, the FR-evaporator can maintain an evaporation rate of about 2.797 kg m^{-2} h^{-1} even in saturated brine under

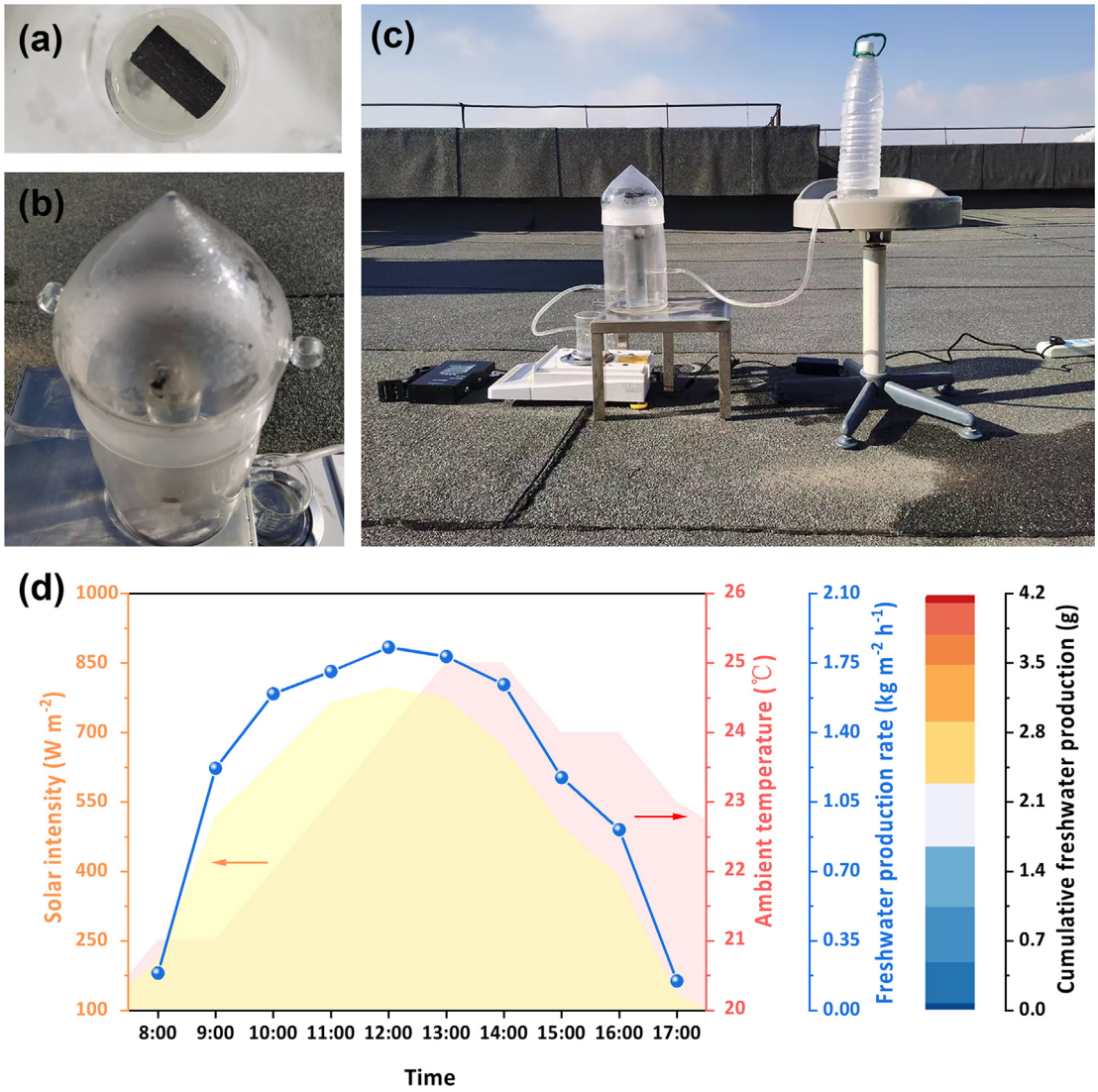

Fig. 5. (Color online) Outdoor test of the C/CuSnS FR-evaporator. (a–c) Digital photos of self-built solar desalination device. (d) Freshwater production rate, cumulative freshwater production of FR-evaporator and conditions in outdoor tests: solar intensity and ambient temperature.

one sun irradiation for 24 h, which has not be achieved by any static evaporator reported before. After 9 h of outdoor solar irradiation, condensed water of 4.11 kg m^{-2} is collected and the water quality meets the drinking water standards of WHO and EPA. Even after 30 days of continuous exposure under one sun (8 h per day), the FR-evaporator shows only an 8% decay in evaporation rate. In a word, our study achieves long-term efficient solar-driven freshwater generation through adaptively rotating salt-removal, providing a scalable solution for solar-driven desalination and wastewater treatment.

Conflict of interest

The authors declare that they have no conflict of interest.

Acknowledgments

This work was supported by the National Natural Science Foundation of China (52272153 and 52032004) and Open Project of Key Laboratory of Optical System Advanced Manufacturing Technology (2022KLOMT02-05).

Author contributions

Hanjin Jiang performed the experiments and wrote the initial manuscript. Xinghang Liu and Dewen Wang designed the experiments and participated in the discussion of the results. Haitao Wang and Yanan Guo characterized the light absorption and hydrophilicity of FR-evaporator. Chaoquan Hu and Dong Wang conceived the project and revised the manuscript. Chaoquan Hu, Gang Gao, and Xiaoyi Wang provided financial support and supervised the project. All authors participated in the preparation of this manuscript.

Appendix A. Supplementary materials

Supplementary materials to this article can be found online at https://doi.org/10.1016/j.scib.2023.07.011.

References

[1] Mekonnen MM, Hoekstra AY. Four billion people facing severe water scarcity. Sci Adv 2016;2:e1500323.
[2] Xu Y, Hu J, Zhang X, et al. Robust and multifunctional natural polyphenolic composites for water remediation. Mater Horiz 2022;9:2496–517.
[3] Zou Y, Wu X, Li H, et al. Metal-phenolic network coated cellulose foams for solar-driven clean water production. Carbohyd Polym 2021;254:117404.
[4] Zhu LL, Gao MM, Peh CKN, et al. Recent progress in solar-driven interfacial water evaporation: advanced designs and applications. Nano Energy 2019;57:507–18.
[5] Zhou L, Li XQ, Ni GW, et al. The revival of thermal utilization from the sun: interfacial solar vapor generation. Natl Sci Rev 2019;6:562–78.
[6] Wang YD, Wu X, Wu P, et al. Enhancing solar steam generation using a highly thermally conductive evaporator support. Sci Bull 2021;66:2479–88.
[7] Zou Y, Zhao JY, Zhu JY, et al. A mussel-inspired polydopamine-filled cellulose aerogel for solar-enabled water remediation. ACS Appl Mater Interfaces 2021;13:7617–24.
[8] Yang P, Bai WJ, Zou Y, et al. A melanin-inspired robust aerogel for multifunctional water remediation. Mater Horiz 2023;10:1020–9.
[9] Wang YD, Wu X, Yang XF, et al. Reversing heat conduction loss: extracting energy from bulk water to enhance solar steam generation. Nano Energy 2020;78:105269.
[10] Tao P, Ni G, Song CY, et al. Solar-driven interfacial evaporation. Nat Energy 2018;3:1031–41.
[11] Zou Y, Chen X, Yang P, et al. Regulating the absorption spectrum of polydopamine. Sci Adv 2020;6:eabb4696.
[12] Yang Y, Yang L, Yang F, et al. A bioinspired antibacterial and photothermal membrane for stable and durable clean water remediation. Mater Horiz 2023;10:268–76.
[13] Gao T, Wang YD, Wu X, et al. More from less: improving solar steam generation by selectively removing a portion of evaporation surface. Sci Bull 2022;67:1572–80.
[14] Wu P, Wu X, Wang YD, et al. Towards sustainable saline agriculture: interfacial solar evaporation for simultaneous seawater desalination and saline soil remediation. Water Res 2022;212:118099.
[15] Chen CJ, Kuang YD, Hu LB. Challenges and opportunities for solar evaporation. Joule 2019;3:683–718.
[16] Zhang LN, Xu ZY, Zhao L, et al. Passive, high-efficiency thermally-localized solar desalination. Energ Environ Sci 2021;14:1771–93.
[17] Zhao D, Xue J, Li S, et al. Theoretical analyses of thermal and economical aspects of multi-effect distillation desalination dealing with high-salinity wastewater. Desalination 2011;273:292–8.
[18] Khawaji AD, Kutubkhanah IK, Wie JM. Advances in seawater desalination technologies. Desalination 2008;221:47–69.
[19] Pugsley A, Zacharopoulos A, Mondol JD, et al. Global applicability of solar desalination. Renew Energ 2016;88:200–19.
[20] Sharaf MA, Nafey AS, Garcia-Rodriguez L. Thermo-economic analysis of solar thermal power cycles assisted MED-VC (multi effect distillation-vapor compression) desalination processes. Energy 2011;36:2753–64.
[21] Semiat R. Energy issues in desalination processes. Environ Sci Technol 2008;42:8193–201.
[22] Zhang X, Yan Y, Li N, et al. A robust and 3D-printed solar evaporator based on naturally occurring molecules. Sci Bull 2023;68:203–13.
[23] Wang YD, Wu X, Gao T, et al. Same materials, bigger output: a reversibly transformable 2D–3D photothermal evaporator for highly efficient solar steam generation. Nano Energy 2021;79:105477.
[24] Wu X, Wu ZQ, Wang YD, et al. All-cold evaporation under one sun with zero energy loss by using a heatsink inspired solar evaporator. Adv Sci 2021;8:2002501.
[25] Zhao W, Gong H, Song Y, et al. Hierarchically designed salt-resistant solar evaporator based on Donnan effect for stable and high-performance brine treatment. Adv Funct Mater 2021;31:2100025.
[26] He S, Chen C, Kuang Y, et al. Nature-inspired salt resistant bimodal porous solar evaporator for efficient and stable water desalination. Energ Environ Sci 2019;12:1558–67.
[27] Zhu L, Sun L, Zhang H, et al. A solution to break the salt barrier for high-rate sustainable solar desalination. Energ Environ Sci 2021;14:2451–9.
[28] Zhang YX, Xiong T, Suresh L, et al. Guaranteeing complete salt rejection by channeling saline water through fluidic photothermal structure toward synergistic zero energy clean water production and in situ energy generation. ACS Energy Lett 2020;5:3397–404.
[29] Ni G, Zandavi SH, Javid SM, et al. A salt-rejecting floating solar still for low-cost desalination. Energ Environ Sci 2018;11:1510–9.
[30] Hu R, Zhang JQ, Kuang YD, et al. A Janus evaporator with low tortuosity for long-term solar desalination. J Mater Chem A 2019;7:15333–40.
[31] Xu N, Li JL, Wang Y, et al. A water lily-inspired hierarchical design for stable and efficient solar evaporation of high-salinity brine. Sci Adv 2019;5:eaaw7013.
[32] Li LX, Zhang JP. Highly salt-resistant and all-weather solar-driven interfacial evaporators with photothermal and electrothermal effects based on Janus graphene@silicone sponges. Nano Energy 2021;81:105682.
[33] Zhang Q, Yi G, Fu Z, et al. Vertically aligned Janus MXene-based aerogels for solar desalination with high efficiency and salt resistance. ACS Nano 2019;13:13196–207.
[34] Yao HZ, Zhang PP, Yang C, et al. Janus-interface engineering boosting solar steam towards high-efficiency water collection. Energ Environ Sci 2021;14:5330.
[35] Wu X, Gao T, Han CH, et al. A photothermal reservoir for highly efficient solar steam generation without bulk water. Sci Bull 2019;64:1625–33.
[36] Yang K, Pan T, Dang S, et al. Three-dimensional open architecture enabling salt-rejection solar evaporators with boosted water production efficiency. Nat Commun 2022;13:6653.
[37] Zhang L, Li X, Zhong Y, et al. Highly efficient and salt rejecting solar evaporation via a wick-free confined water layer. Nat Commun 2022;13:849.
[38] Zou M, Zhang Y, Cai Z, et al. 3D printing a biomimetic bridge-arch solar evaporator for eliminating salt accumulation with desalination and agricultural applications. Adv Mater 2021;33:2102443.
[39] Liu X, Chen F, Li Y, et al. 3D hydrogel evaporator with vertical radiant vessels breaking the trade-off between thermal localization and salt resistance for solar desalination of high-salinity. Adv Mater 2022;34:2203137.
[40] Chaule S, Hwang J, Ha SJ, et al. Rational design of a high performance and robust solar evaporator via 3D-printing technology. Adv Mater 2021;33:2102649.
[41] Sun Y, Zhao ZB, Zhao GY, et al. High performance carbonized corncob-based 3D solar vapor steam generator enhanced by environmental energy. Carbon 2021;179:337–47.
[42] Koh JJ, Lim GJH, Chakraborty S, et al. Robust, 3D-printed hydratable plastics for effective solar desalination. Nano Energy 2021;79:105436.
[43] Fan XQ, Yang Y, Shi XL, et al. A MXene-based hierarchical design enabling highly efficient and stable solar-water desalination with good salt resistance. Adv Funct Mater 2020;30:2007110.
[44] Tian YK, Li YJ, Zhang XY, et al. Breath-figure self-assembled low-cost Janus fabrics for highly efficient and stable solar desalination. Adv Funct Mater 2022;32:2113258.
[45] Wang ZX, Wu XC, He F, et al. Confinement capillarity of thin coating for boosting solar-driven water evaporation. Adv Funct Mater 2021;31:2011114.
[46] Wu L, Dong Z, Cai Z, et al. Highly efficient three-dimensional solar evaporator for high salinity desalination by localized crystallization. Nat Commun 2020;11:521.

[47] Peng HY, Wang D, Fu SH. Artificial transpiration with asymmetric photothermal textile for continuous solar-driven evaporation, spatial salt harvesting and electrokinetic power generation. Chem Eng J 2021;426:131818.
[48] Liu CK, Peng Y, Zhao XZ. Continuous solar desalination based on restricted salt crystallization zone. Desalination 2021;501:114911.
[49] Lei ZW, Sun XT, Zhu SF, et al. Nature inspired MXene-decorated 3D honeycomb-fabric architectures toward efficient water desalination and salt harvesting. Nano Micro Lett 2022;14:10.
[50] Wang Z, Gao J, Zhou J, et al. Engineering metal-phenolic networks for solar desalination with directional salt crystallization. Adv Mater 2023;35:2209015.
[51] Xia Y, Hou QF, Jubaer H, et al. Spatially isolating salt crystallisation from water evaporation for continuous solar steam generation and salt harvesting. Energ Environ Sci 2019;12:1840–7.
[52] Wang Y, Sun X, Tao S. Rational 3D coiled morphology for efficient solar-driven desalination. Environ Sci Technol 2020;54:16240–8.
[53] Wang YD, Wu X, Shao B, et al. Boosting solar steam generation by structure enhanced energy management. Sci Bull 2020;65:1380–8.
[54] Finnerty C, Zhang L, Sedlak DL, et al. Synthetic graphene oxide leaf for solar desalination with zero liquid discharge. Environ Sci Technol 2017;51:11701–9.
[55] Xia Y, Li Y, Yuan S, et al. A self-rotating solar evaporator for continuous and efficient desalination of hypersaline brine. J Mater Chem A 2020;8:16212–7.
[56] Xu N, Zhang H, Lin Z, et al. A scalable fish-school inspired self-assembled particle system for solar-powered water-solute separation. Natl Sci Rev 2021;8:nwab065.
[57] Wu X, Wang Y, Wu P, et al. Dual-zone photothermal evaporator for antisalt accumulation and highly efficient solar steam generation. Adv Funct Mater 2021;31:2102618.
[58] Zhang H, Shen X, Kim E, et al. Integrated water and thermal managements in bioinspired hierarchical MXene aerogels for highly efficient solar-powered water evaporation. Adv Funct Mater 2022;32:2111794.
[59] Metwally S, Comesaña SM, Zarzyka M, et al. Thermal insulation design bioinspired by microstructure study of penguin feather and polar bear hair. Acta Biomater 2019;91:270–83.
[60] Guo S, Li X, Li J, et al. Boosting photocatalytic hydrogen production from water by photothermally induced biphase systems. Nat Commun 2021;12:1343.
[61] Kuang Y, Chen C, He S, et al. A high-performance self-regenerating solar evaporator for continuous water desalination. Adv Mater 2019;31:1900498.
[62] Chen X, He S, Falinski MM, et al. Sustainable off-grid desalination of hypersaline waters using Janus wood evaporators. Energ Environ Sci 2021;14:5347–57.
[63] Zhu MW, Li YJ, Chen G, et al. Tree-inspired design for high-efficiency water extraction. Adv Mater 2017;29:1704107.
[64] Lu Y, Fan DQ, Shen ZY, et al. Design and performance boost of a MOF-functionalized-wood solar evaporator through tuning the hydrogen-bonding interactions. Nano Energy 2022;95:107016.
[65] Wu X, Robson ME, Phelps JL, et al. A flexible photothermal cotton-CuS nanocage-agarose aerogel towards portable solar steam generation. Nano Energy 2019;56:708–15.
[66] Wang ZG, Yu K, Gong SJ, et al. Cu_3BiS_3/MXenes with excellent solar-thermal conversion for continuous and efficient seawater desalination. ACS Appl Mater Interfaces 2021;13:16246–58.
[67] Zhu RF, Liu MM, Hou YY, et al. Mussel-inspired photothermal synergetic system for clean water production using full-spectrum solar energy. Chem Eng J 2021;423:129099.
[68] Zheng X, Wang H, Ye F, et al. Organic-inorganic hybrid hole transport layers with sns doping boost the performance of perovskite solar cells. J Energy Chem 2022;68:637–45.
[69] Hatch CD, Christie MJ, Weingold RM, et al. Horizontal attenuated total reflectance Fourier transform infrared and X-ray photoelectron spectroscopy measurements of water adsorption on oxidized tin (II) sulfide (SnS) surfaces. J Phys Chem C 2013;117:472–82.
[70] Gao M, Zhu L, Peh CK, et al. Solar absorber material and system designs for photothermal water vaporization towards clean water and energy production. Energ Environ Sci 2019;12:841–6.
[71] Jiang H, Liu X, Wang D, et al. Designing high-efficiency light-to-thermal conversion materials for solar desalination and photothermal catalysis. J Energy Chem 2023;79:581–600.
[72] Indriyati PI, Permatasari FA, et al. Recent advances and rational design strategies of carbon dots towards highly efficient solar evaporation. Nanoscale 2021;13:7523–32.
[73] Tao F, Zhang Y, Yin K, et al. Copper sulfide-based plasmonic photothermal membrane for high-efficiency solar vapor generation. ACS Appl Mater Interfaces 2018;10:35154–63.
[74] Yu F, Guo Z, Xu Y, et al. Biomass-derived bilayer solar evaporator with enhanced energy utilization for high-efficiency water generation. ACS Appl Mater Interfaces 2021;12:57155–64.
[75] Guo Y, Dundas CM, Zhou X, et al. Molecular engineering of hydrogels for rapid water disinfection and sustainable solar vapor generation. Adv Mater 2021;33:2102994.
[76] Hu Y, Ma H, Wu M, et al. A reconfigurable and magnetically responsive assembly for dynamic solar steam generation. Nat Commun 2022;13:4335.
[77] Menon AK, Haechler I, Kaur S, et al. Enhanced solar evaporation using a photothermal umbrella for wastewater management. Nat Sustain 2020;3:144–51.
[78] Zhang C, Shi Y, Shi L, et al. Designing a next generation solar crystallizer for real seawater brine treatment with zero liquid discharge. Nat Commun 2021;12:998.
[79] Shi Y, Ilic O, Atwater HA, et al. All-day fresh water harvesting by microstructured hydrogel membranes. Nat Commun 2021;12:2797.
[80] Dong X, Cao L, Si Y, et al. Cellular structured CNTs@SiO_2 nanofibrous aerogels with vertically aligned vessels for salt-resistant solar desalination. Adv Mater 2020;32:1908269.
[81] Chen X, Yang N, Wang Y, et al. Highly efficient photothermal conversion and water transport during solar evaporation enabled by amorphous hollow multishelled nanocomposites. Adv Mater 2022;34:2107400.
[82] Li H, Zhu W, Li M, et al. Side area-assisted 3D evaporator with antibiofouling function for ultra-efficient solar steam generation. Adv Mater 2021;33:2102258.
[83] Zhou X, Guo Y, Zhao F, et al. Topology-controlled hydration of polymer network in hydrogels for solar-driven wastewater treatment. Adv Mater 2020;32:2007012.
[84] Zou H, Meng X, Zhao X, et al. Hofmeister effect-enhanced hydration chemistry of hydrogel for high-efficiency solar-driven interfacial desalination. Adv Mater 2022;35:2207262.
[85] Andrews FC. Colligative properties of simple solutions. Science 1976;194:567–71.
[86] Qiu Y, Zhou Z, Zhang C, et al. Confined shape-morphing and dual hydration modes for efficient solar steam generation. ACS Energy Lett 2022;7:3476–83.
[87] Chen J, Yin JL, Li B, et al. Janus evaporators with self-recovering hydrophobicity for salt-rejecting interfacial solar desalination. ACS Nano 2020;14:17419–27.
[88] Qiu Y, Lee M, Chen J, et al. Effect of light intensity on solar-driven interfacial steam generation. Nanoscale 2021;13:20387.

Hanjin Jiang is a Ph.D. candidate under the supervision of Prof. Chaoquan Hu and associate Prof. Dong Wang at School of Materials Science and Engineering, Jilin University. Her research interest focuses on development and application of light-to-thermal conversion materials.

Dong Wang is an associate professor at College of Chemical Engineering, Northeast Electric Power University. He received his Ph.D. degree from the State Key Laboratory of Inorganic Synthesis and Preparative Chemistry, Jilin University. He was engaged in post-doctoral research at Stockholm University from 2011 to 2012. His current research activities involve design and preparation of photothermal conversion materials and gas sensing materials.

Gang Gao is an assistant professor at School of Astronautics, Harbin Institute of Technology. He received his Ph.D. degree from Harbin Institute of Technology in 2022. He worked as a joint doctoral student at National University of Singapore from 2020 to 2021. His current research interest includes transparent semiconductor films, transparent display devices, on-chip integrated infrared optoelectronic communication and detector.

Xiaoyi Wang is a researcher of Changchun Institute of Optics, Fine Mechanics and Physics, Chinese Academy of Sciences. He received his master's degree from State Key Laboratory of Superhard Materials, Jilin University. He has engaged in optical film, thin film dispersion elements, and nanostructure surface research.

Chaoquan Hu is a professor at School of Materials Science and Engineering, Jilin University. He received his Ph.D. degree from Jilin University in 2007. He was engaged in postdoctoral research at Harbin Institute of Technology from 2007 to 2010. He worked as a visiting scholar at Nanyang Technological University from 2014 to 2015. He has long been engaged in research on optical films and photothermal conversion materials.